

Supporting Information

Effects of coordination sphere on unusually large zero field splitting and slow magnetic relaxation in trigonally symmetric molecules

Kelsey A. Schulte,^a Kuduva R. Vignesh,^a and Kim R. Dunbar^{*a}

^aDepartment of Chemistry, Texas A&M University, College Station, Texas 77843, USA.

Corresponding author: Kim R. Dunbar, email: dunbar@chem.tamu.edu

Table of Contents:

Experimental Details	S2
Single Crystal X-ray Diffraction	S4
Static DC Measurements	S8
Dynamic AC Susceptibility Measurements	S17
Computational Details	S22
References	S26

Experimental:

All syntheses were conducted under a N₂ atmosphere. Anhydrous complexes were synthesized in an MBRAUN glovebox under rigorous anhydrous conditions. The synthesis of the water complexes took place in a Vacuum Atmosphere glovebox with the catalyst turned off so that it was not a totally dry atmosphere. Commercial anhydrous dimethylacetamide (DMA) was dried over BaO, and stored in the drybox over molecular sieves. Diethyl ether was purified using an MBRAUN purification system and stored over 3Å molecular sieves. Dichloromethane (DCM) was dried over P₂O₅ and stored over 3Å molecular sieves. Diethyl ether and dichloromethane in the purge box were degassed with an Argon stream. Co(OAc)₂, Fe(OAc)₂ and NaH were purchased and used as received. Ni(OAc)₂•4H₂O and Me₄NOAc were dried under vacuum at 100°C overnight. Dryness was confirmed for each of these starting materials using infrared spectroscopy. The ligand H₃[MST] was synthesized according to literature procedures.¹ Syntheses of the (Me₄N)[M^{II}(MST)] and (Me₄N)[M^{II}(MST)(OH₂)] complexes were performed with modified procedures from literature;¹⁻³ details are below.

(Me₄N)[Co(MST)] (**1**). A 20 mL vial was charged with H₃[MST] (300 mg, 0.43 mmol), NaH (31.2 mg, 1.30 mmol), Me₄NOAc (86.4 mg, 0.65 mmol), and DMA (5 mL). The reaction was stirred until all of the NaH had reacted. Co(OAc)₂ (76.5 mg, 0.43 mmol) was added to the reaction and the mixture was stirred for overnight to give a dark pink solution which was subsequently filtered over a fine frit. Crystals were obtained via diethyl ether diffusion into the DMA solution. The crystals were further purified by dissolution in dichloromethane and filtration over a fine frit. Slow diffusion of diethyl ether resulted in sky blue crystals (181 mg, 51% yield). Analysis calculated for (Me₄N)[Co(MST)] (C₃₇H₅₇CoN₅O₆S₃): C: 54.00%, H: 6.98%, N: 8.51%. Found: C: 53.77%, H: 7.25%, N: 8.31%.

(Me₄N)[Co(MST)(OH₂)]•DCM (**2**). Crystals of **1** were dissolved in dichloromethane and water was added dropwise to the rapidly stirring solution until it turned bright pink. Slow diffusion of diethyl ether resulted in the isolation of pink crystals (166 mg, 90% yield). Analysis calculated for (Me₄N)[Co(MST)(OH₂)]•DCM (C₃₈H₆₁Cl₂CoN₅O₇S₃): C: 49.29%, H: 6.64%, N: 7.56%. Found: C: 49.53%, H: 6.64%, N: 7.64%.

(Me₄N)[Fe(MST)] (**3**). **3** was synthesized in a manner akin to **1** using Fe(OAc)₂ (74.8 mg, 0.43 mmol), H₃[MST] (300 mg, 0.43 mmol), NaH (31.2 mg, 1.30 mmol), Me₄NOAc (86.4 mg, 0.65 mmol), and DMA (5 mL). Pale yellow-to-colorless crystals suitable for x-ray analysis were obtained via slow diffusion of diethyl ether into the original DMA solution (194 mg, 55% yield). Analysis calculated for (Me₄N)[Fe(MST)] (C₃₇H₅₇FeN₅O₆S₃): C: 54.20%, H: 7.01%, N: 8.54%. Found: C: 54.38%, H: 7.28%, N: 8.03%.

(Me₄N)[Fe(MST)(OH₂)] (**4**). To a solution of **3** in DMA was added 10 µL of water. Pale yellow crystals suitable for x-ray analysis were obtained via slow diffusion of diethyl ether into the DMA solution (172 mg, 87% yield). Analysis calculated for (Me₄N)[Fe(MST)(OH₂)] (C₃₇H₅₇FeN₅O₆S₃): C: 52.04%, H: 7.10%, N: 6.66%. Found: C: 52.85%, H: 7.32%, N: 8.09%.

(Me₄N)[Ni(MST)] (**5**). **5** was synthesized in a manner analogous to **1** using Ni(OAc)₂ (76.0 mg, 0.43 mmol), H₃[MST] (300 mg, 0.43 mmol), NaH (31.2 mg, 1.30 mmol), Me₄NOAc (86.4 mg,

0.65 mmol), and DMA (5 mL). Salmon colored crystals suitable for x-ray analysis were obtained via slow diffusion of diethyl ether into the original DMA solution (134 mg, 38% yield). Analysis calculated for $(\text{Me}_4\text{N})[\text{Ni}(\text{MST})]$ ($\text{C}_{37}\text{H}_{57}\text{NiN}_5\text{O}_6\text{S}_3$): C: 54.01%, H: 6.98%, N: 8.51%. Found: C: 54.24%, H: 6.75%, N: 8.21%. Yield can be increased by adding DCM to the solid which was collected by filtration and re-filtering the orange solution. Crystals were grown via slow diffusion of diethyl ether into the DCM solution (184mg, 52% total yield).

$(\text{Me}_4\text{N})[\text{Ni}(\text{MST})(\text{OH}_2)]$ (**6**). To a stirred solution of **5** in DMA, water was added dropwise until the solution turned green. Green crystals suitable for x-ray analysis were obtained via slow diffusion of diethyl ether into the DMA solution (175 mg, 93% yield). Analysis calculated for $(\text{Me}_4\text{N})[\text{Ni}(\text{MST})(\text{OH}_2)]\cdot\text{H}_2\text{O}$ ($\text{C}_{37}\text{H}_{57}\text{NiN}_5\text{O}_6\text{S}_3$): C: 51.75%, H: 7.16%, N: 8.16%. Found: C: 51.38%, H: 7.54%, N: 7.77%.

Crystallography

Structural characterization was performed with single crystals on Bruker QUEST and VENTURE instruments with Mo K α and microfocus Cu K α sources respectively. Compounds **1**, **2**, and **6** were collected on the VENTURE instrument equipped with a CMOS detector and **3**, **4**, and **5** were collected on the QUEST instrument equipped with a CCD detector. Suitable crystals were mounted on MiTeGen microloops using Paratone oil and placed in a cold stream of N_2 for collection at 110 K. The collected data was integrated within the APEX 2 software suite, as well as SADABS for absorbance corrections.⁴ The structures were solved and refined using SHELXT⁵ and SHELXL⁶ respectively within the OLEX program.⁷ Hydrogen atoms were added in calculated positions. In some cases, reorientations of hydrogen atoms was performed to match visible electron density as well as due to obvious hydrogen bonding interactions.

All non-hydrogen atoms were refined anisotropically, with the exception of disordered solvent in **2**. The structure of **2** exhibits disordered dichloromethane over two positions in a ratio of 85:15. The major component of the disorder could be modelled anisotropically, whereas the minor component could only be refined isotropically. The SIMU and SADI restraints were necessary in order to achieve a reasonable model of the disorder. Structures **4** and **6** exhibit disorder in the $[\text{Me}_4\text{N}]^+$ cation. For **4**, three of the methyl groups rotate around an axis between the central carbon and remaining methyl group. The two parts exist in a 51:49 ratio. The same type of disorder exists in **6**, but with one orientation being preferred 77% of the time. Cambridge crystallographic numbers for each of the compounds are as follows: $(\text{Me}_4\text{N})[\text{Co}(\text{MST})]$ (Me_4N) 1851169, $[\text{Co}(\text{MST})(\text{OH}_2)]$ 1851168, $(\text{Me}_4\text{N})[\text{Fe}(\text{MST})]$ 1851170, $(\text{Me}_4\text{N})[\text{Fe}(\text{MST})(\text{OH}_2)]$ 1851172, $(\text{Me}_4\text{N})[\text{Ni}(\text{MST})]$ 1851171, and $(\text{Me}_4\text{N})[\text{Ni}(\text{MST})(\text{OH}_2)]$ 1851173.

Magnetic Measurements

Magnetic data was collected on a Quantum Design MPMS-3 SQUID. Data were collected from 1.8-300 K with DC fields from 0-7T. Compounds **1-4**, **6** were collected in plastic bags and compound **5** was collected in an NMR tube under a coating of eicosaine. Diamagnetic corrections were applied for the bags, NMR tube, and eicosaine. The diamagnetic contribution from the compounds were calculated based on Pascal's constants.⁸

Crystallography Tables:

Table S1: Crystal structure data and refinement parameters for (Me₄N)[M^{II}(MST)] and (Me₄N)[M^{II}(MST)(OH₂)] complexes.

Identification code	(Me ₄ N)[Co(MST)]	(Me ₄ N)[Co(MST)(OH ₂)]
Empirical formula	C ₃₇ H ₅₇ CoN ₅ O ₆ S ₃	C ₃₈ H ₆₃ Cl ₂ CoN ₅ O ₈ S ₃
Formula weight	822.98	943.94
Temperature/K	100	100
Crystal system	monoclinic	triclinic
Space group	P2 ₁ /n	P-1
a/Å	21.1512(8)	8.8767(7)
b/Å	9.0244(4)	14.5893(11)
c/Å	21.2686(9)	19.0022(14)
α/°	90	107.139(2)
β/°	95.072(2)	97.232(2)
γ/°	90	101.356(2)
Volume/Å ³	4043.8(3)	2260.7(3)
Z	4	2
ρ _{calc} /g/cm ³	1.352	1.387
μ/mm ⁻¹	5.18	5.799
F(000)	1748	998
Crystal size/mm ³	0.693 × 0.079 × 0.036	0.548 × 0.103 × 0.088
Radiation	CuKα (λ = 1.54178)	CuKα (λ = 1.54178)
2θ range for data collection/°	5.648 to 130.166	4.962 to 136.062
Index ranges	-24 ≤ h ≤ 24, -10 ≤ k ≤ 10, -24 ≤ l ≤ 24	-10 ≤ h ≤ 10, -17 ≤ k ≤ 17, -22 ≤ l ≤ 22
Reflections collected	44132	26923
Independent reflections	6898 [R _{int} = 0.0598, R _{sigma} = 0.0375]	7962 [R _{int} = 0.0391, R _{sigma} = 0.0366]
Data/restraints/parameters	6898/0/482	7962/50/544
Goodness-of-fit on F ² ^c	1.044	1.057
Final R indexes [I >= 2σ (I)] ^{a,b}	R ₁ = 0.0413, wR ₂ = 0.0912	R ₁ = 0.0477, wR ₂ = 0.1232
Final R indexes [all data] ^{a,b}	R ₁ = 0.0566, wR ₂ = 0.0984	R ₁ = 0.0499, wR ₂ = 0.1246
Largest diff. peak/hole / e Å ⁻³	0.64/-0.52	0.45/-0.90

Table S1: Crystal structure data and refinement parameters for (Me₄N)[M^{II}(MST)] and (Me₄N)[M^{II}(MST)(OH₂)] complexes continued.

	(Me ₄ N)[Fe(MST)]	(Me ₄ N)[Fe(MST)(OH ₂)]
Identification code	(Me ₄ N)[Fe(MST)]	(Me ₄ N)[Fe(MST)(OH ₂)]
Empirical formula	C ₃₇ H ₅₇ FeN ₅ O ₆ S ₃	C ₃₇ H ₅₉ FeN ₅ O ₇ S ₃
Formula weight	819.9	837.92
Temperature/K	100	100
Crystal system	monoclinic	monoclinic
Space group	P2 ₁ /n	C2/c
a/Å	21.1950(6)	26.6560(8)
b/Å	9.0313(3)	9.6645(3)
c/Å	21.2797(6)	31.5226(9)
α/°	90	90
β/°	94.9100(10)	90.4400(10)
γ/°	90	90
Volume/Å ³	4058.4(2)	8120.5(4)
Z	4	8
ρ _{calc} /cm ³	1.342	1.371
μ/mm ⁻¹	0.576	0.579
F(000)	1744	3568
Crystal size/mm ³	0.21 × 0.209 × 0.121	0.584 × 0.134 × 0.129
Radiation	Mo Kα (λ = 0.71073)	MoKα (λ = 0.71073)
2θ range for data collection/°	4.902 to 51.482	4.484 to 56.73
Index ranges	-24 ≤ h ≤ 24, -10 ≤ k ≤ 10, -25 ≤ l ≤ 25	-35 ≤ h ≤ 35, -12 ≤ k ≤ 12, -41 ≤ l ≤ 41
Reflections collected	85488	132799
Independent reflections	7470 [R _{int} = 0.0482, R _{sigma} = 0.0274]	9986 [R _{int} = 0.0581, R _{sigma} = 0.0339]
Data/restraints/parameters	7470/0/482	9986/0/523
Goodness-of-fit on F ² ^c	1.118	1.081
Final R indexes [I ≥ 2σ (I)] ^{a,b}	R ₁ = 0.0412, wR ₂ = 0.0904	R ₁ = 0.0388, wR ₂ = 0.0902
Final R indexes [all data] ^{a,b}	R ₁ = 0.0550, wR ₂ = 0.0947	R ₁ = 0.0553, wR ₂ = 0.0965
Largest diff. peak/hole / e Å ⁻³	0.44/-0.44	0.49/-0.49

Table S1: Crystal structure data and refinement parameters for (Me₄N)[M^{II}(MST)] and (Me₄N)[M^{II}(MST)(OH₂)] complexes continued.

Identification code	(Me ₄ N)[Ni(MST)]	(Me ₄ N)[Ni(MST)(OH ₂)]
Empirical formula	C ₃₇ H ₅₇ N ₅ NiO ₆ S ₃	C ₃₉ H ₆₆ N ₅ NiO _{8.5} S ₃
Formula weight	822.76	895.85
Temperature/K	100	100
Crystal system	monoclinic	triclinic
Space group	P2 ₁ /n	P-1
a/Å	21.0944(17)	8.9571(7)
b/Å	8.9422(8)	14.5969(11)
c/Å	21.3506(17)	18.6587(14)
α/°	90	107.6400(10)
β/°	94.977(2)	99.2520(10)
γ/°	90	103.1570(10)
Volume/Å ³	4012.2(6)	2193.3(3)
Z	4	2
ρ _{calc} /cm ³	1.362	1.356
μ/mm ⁻¹	0.69	2.432
F(000)	1752	958
Crystal size/mm ³	0.207 × 0.096 × 0.027	0.322 × 0.213 × 0.163
Radiation	Mo Kα (λ = 0.71073)	CuKα (λ = 1.54178)
2θ range for data collection/°	4.942 to 50.974	5.13 to 144.956
Index ranges	-24 ≤ h ≤ 25, -10 ≤ k ≤ 10, -25 ≤ l ≤ 25	-11 ≤ h ≤ 11, -18 ≤ k ≤ 17, -23 ≤ l ≤ 22
Reflections collected	65547	33214
Independent reflections	7410 [R _{int} = 0.1191, R _{sigma} = 0.0572]	8550 [R _{int} = 0.0206, R _{sigma} = 0.0170]
Data/restraints/parameters	7410/0/482	8550/75/582
Goodness-of-fit on F ^{2c}	1.156	1.056
Final R indexes [I ≥ 2σ (I)] ^{a,b}	R ₁ = 0.0904, wR ₂ = 0.2314	R ₁ = 0.0295, wR ₂ = 0.0787
Final R indexes [all data] ^{a,b}	R ₁ = 0.1162, wR ₂ = 0.2436	R ₁ = 0.0309, wR ₂ = 0.0818
Largest diff. peak/hole / e Å ⁻³	1.35/-0.95	0.35/-0.42

^aR₁ = Σ(|F_o| - |F_c|)/Σ|F_o|. ^bwR₂ = [Σ[w(F_o² - F_c²)²]/Σ[w(F_o²)²]^{1/2} ^cGoodness-of-fit = {Σ[w(F_o² - F_c²)²]/(n - p)}^{1/2}, where n is the number of reflections and p is the total number of parameters refined.

Table S2. Selected bond lengths and angles around the inner coordination sphere of **1-6**.

	1	2	3	4	5	6
N1	2.118(2)	2.180(2)	2.165(2)	2.2495(14)	2.035(6)	2.0885(11)
N2	1.972(2)	2.032(2)	2.018(2)	2.0692(15)	1.965(6)	2.0311(12)
N3	1.969(2)	2.033(3)	2.002(2)	2.0981(15)	1.984(6)	2.0254(12)
N4	1.959(2)	2.022(2)	2.018(2)	2.0564(15)	1.998(6)	2.0383(12)
N2-M-N3	117.56(10)	120.04(10)	118.34(9)	116.66(6)	122.5(3)	108.42(5)
N3-M-N4	118.83(10)	114.81(10)	119.99(9)	120.84(6)	116.2(3)	128.98(5)
N4-M-N2	120.34(10)	118.90(10)	116.71(9)	113.74(6)	119.4(3)	118.00(5)
N1-M-O7		176.72(9)		171.74(5)		178.44(4)

Table S3. Selected intermolecular and intramolecular distance of **1-6**.

	1	3	5	2	4	6
$N_3 \dots M^a$	0.207	0.261	0.159	0.295	0.358	0.222
$M \dots M^b$	8.508	8.588	8.423	8.479	8.427	8.356

^a distance between the metal center and the plane generated by the three equatorially coordinated nitrogen atoms (N2-N4)

^b closest intermolecular distance between two metal centers

Table S4. Shape measurements for compounds **1-6**. Abbreviations are as follows: SP, square; T, tetrahedron; SS, seesaw; vTBPY, axially vacant trigonal bipyramid; PP, pentagon; vOC, vacant octahedron; TBPY, trigonal bipyramid; SPY, square pyramid; JTBPY, Johnson trigonal bipyramid.

	SP	T	SS	vTBPY	PP	vOC	TBPY	SPY	JTBPY
1	35.505	5.094	8.176	0.233					
3	35.555	5.675	8.338	0.350					
5	34.630	5.046	7.822	0.176					
2					35.541	7.083	0.695	5.309	2.498
4					34.330	7.205	1.050	5.154	2.770
6					33.794	5.213	0.669	3.966	3.135

Magnetization at 1.8 K

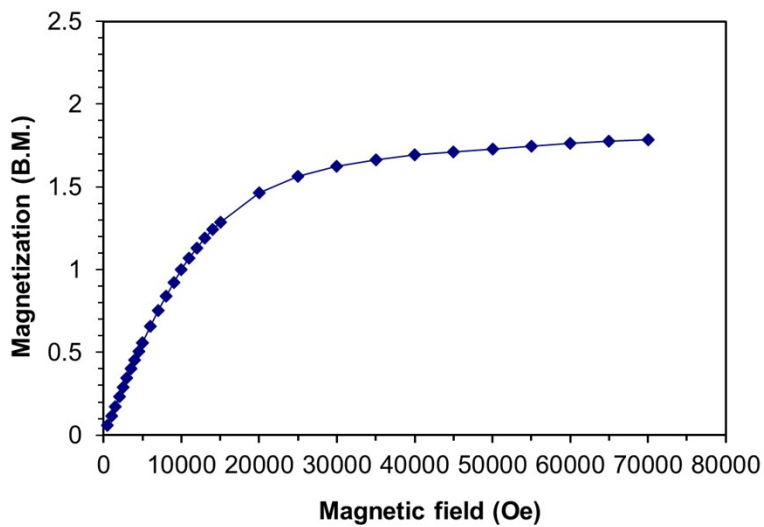


Figure S1. Magnetization vs Field for **1**. Solid lines are guides for the eye.

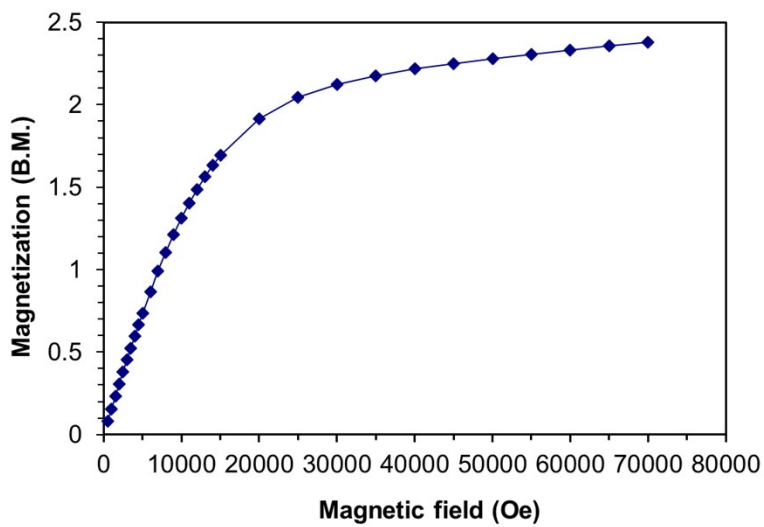


Figure S2. Magnetization vs Field for **2**. Solid lines are guides for the eye.

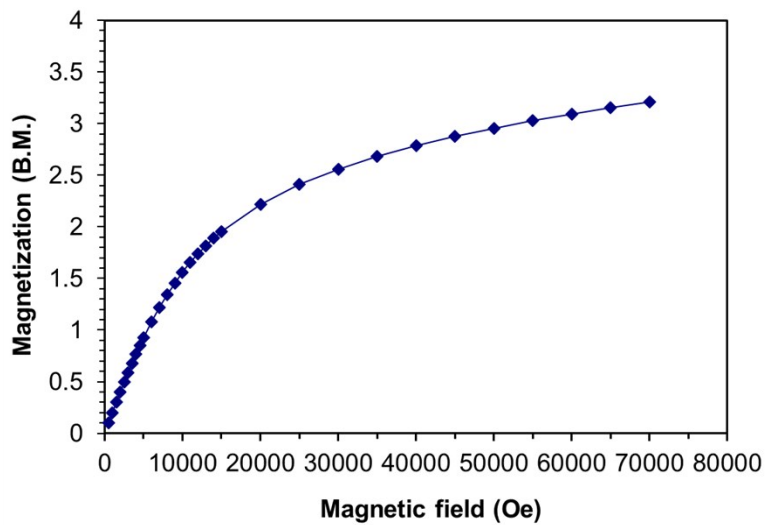


Figure S3. Magnetization vs Field for 3. Solid lines are guides for the eye.

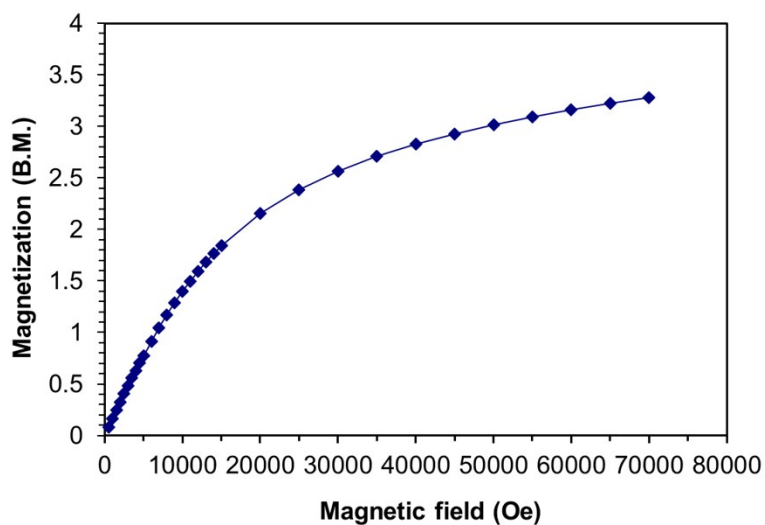


Figure S4. Magnetization vs Field for 4. Solid lines are guides for the eye.

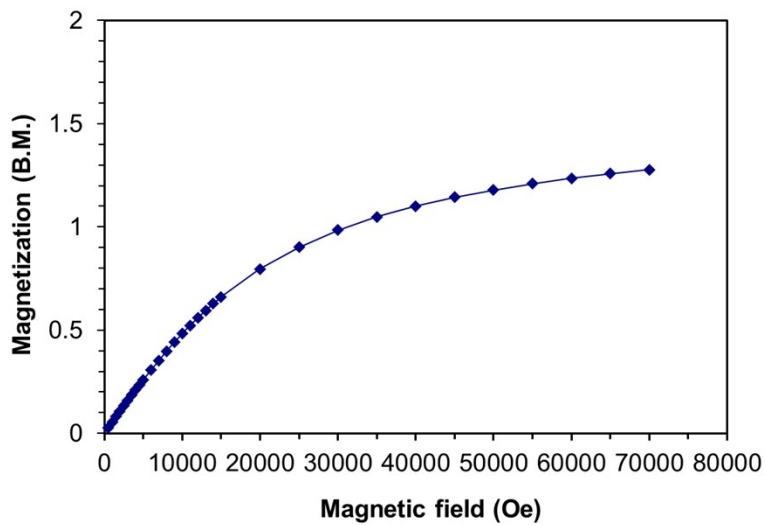


Figure S5. Magnetization vs Field for **5**. Solid lines are guides for the eye.

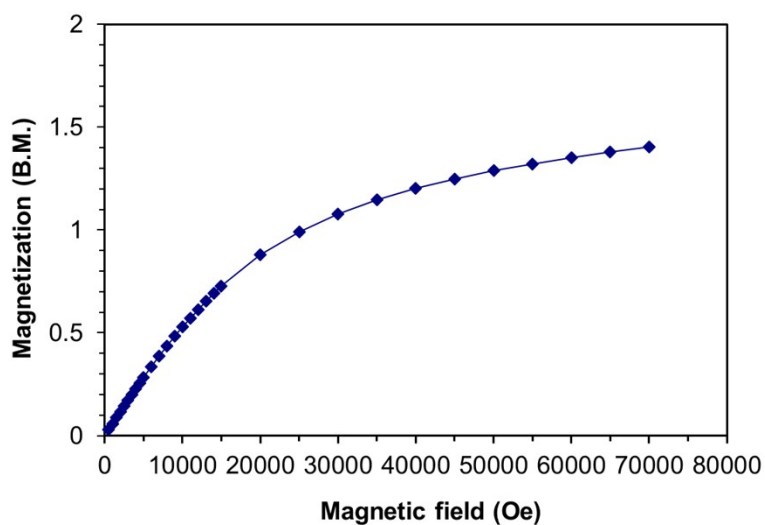


Figure S6. Magnetization vs Field for **6**. Solid lines are guides for the eye.

Reduced Magnetization

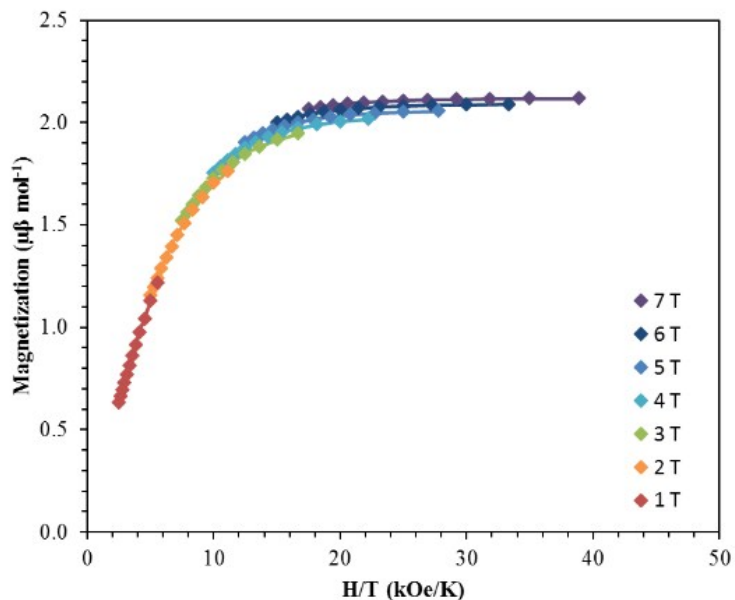


Figure S7. Reduced magnetization for **1**. Solid lines are fits to the experimental data using PHI.

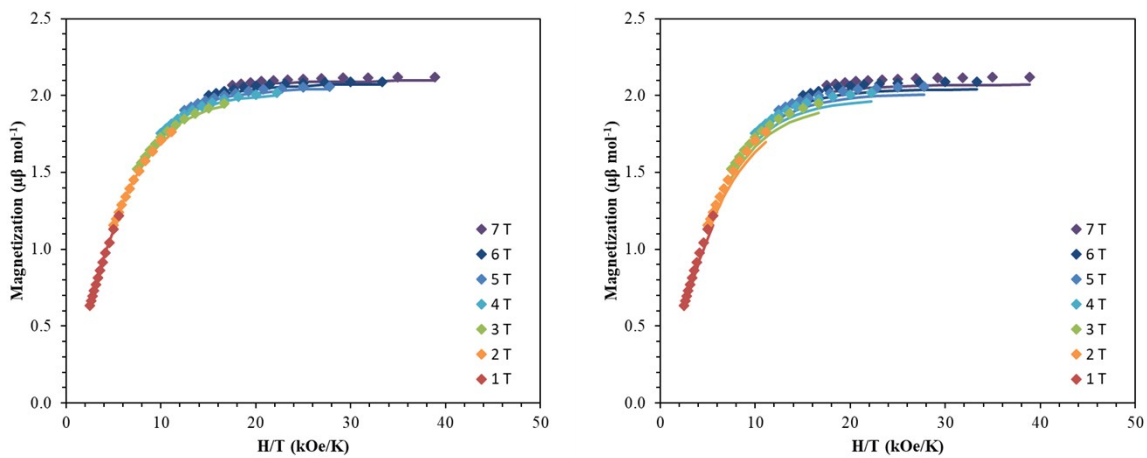


Figure S8. Reduced magnetization for **1**. Solid lines are simulations of CASSCF (left) and NEVPT2 (right) computational results.

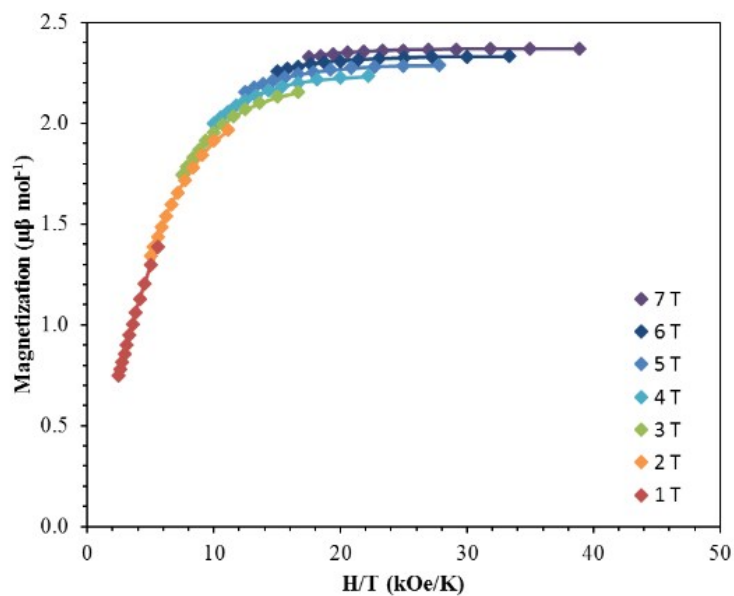


Figure S9. Reduced magnetization for **2**. Solid lines are fits to the experimental data using PHF.

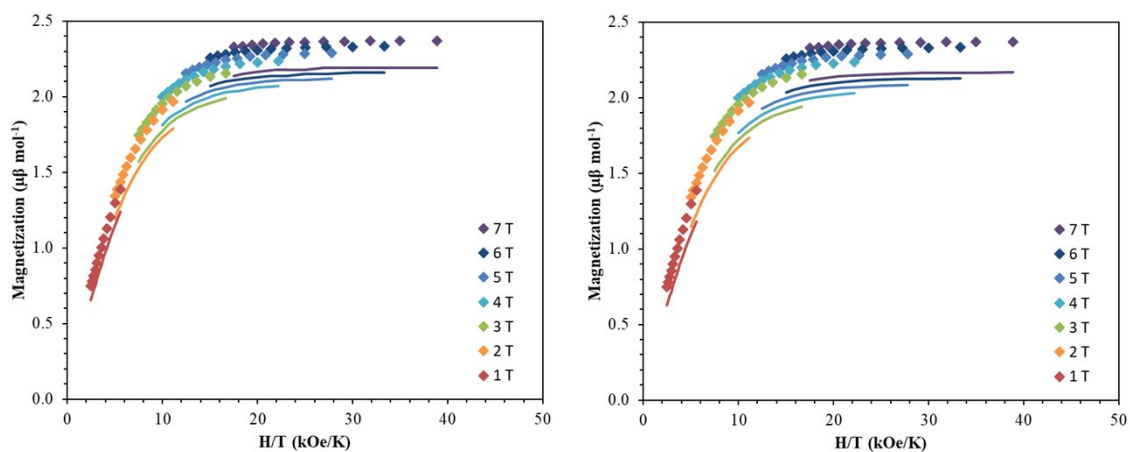


Figure S10. Reduced magnetization for **2**. Solid lines are simulations of CASSCF (left) and NEVPT2 (right) computational results.

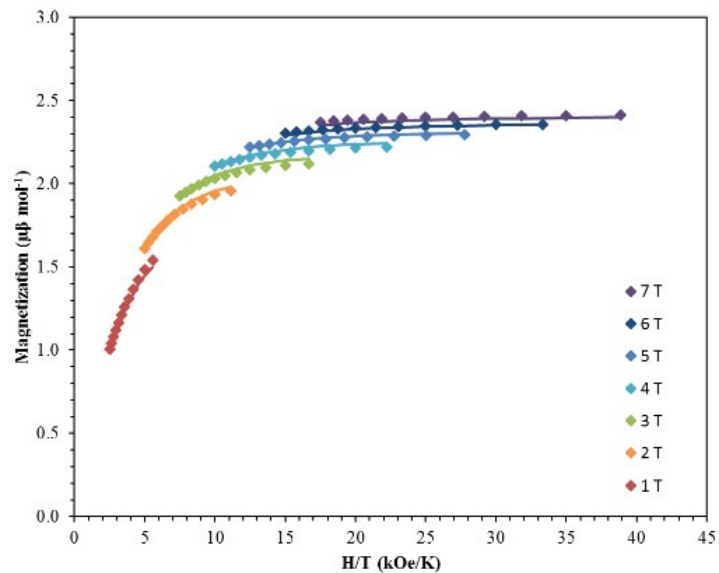


Figure S11. Reduced magnetization for **3**. Solid lines are fits to the experimental data using PHI.

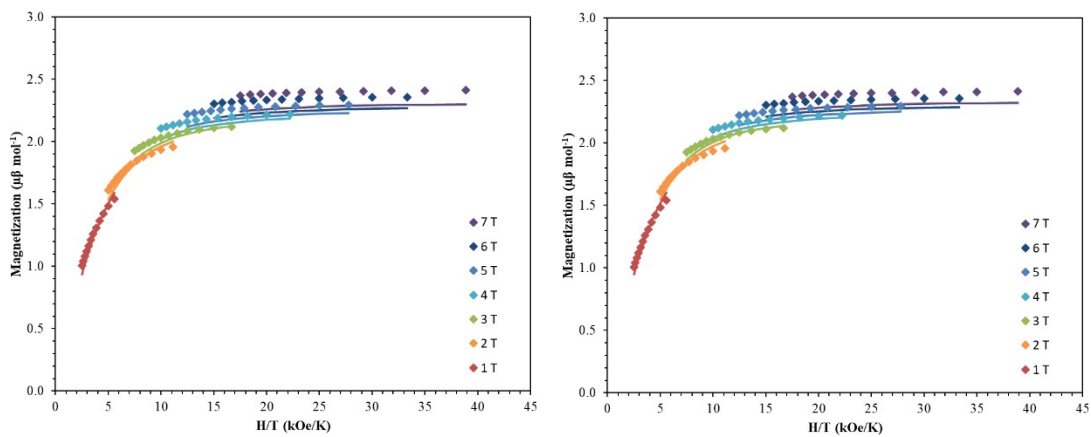


Figure S12. Reduced magnetization for **3**. Solid lines are simulations of CASSCF (left) and NEVPT2 (right) computational results.

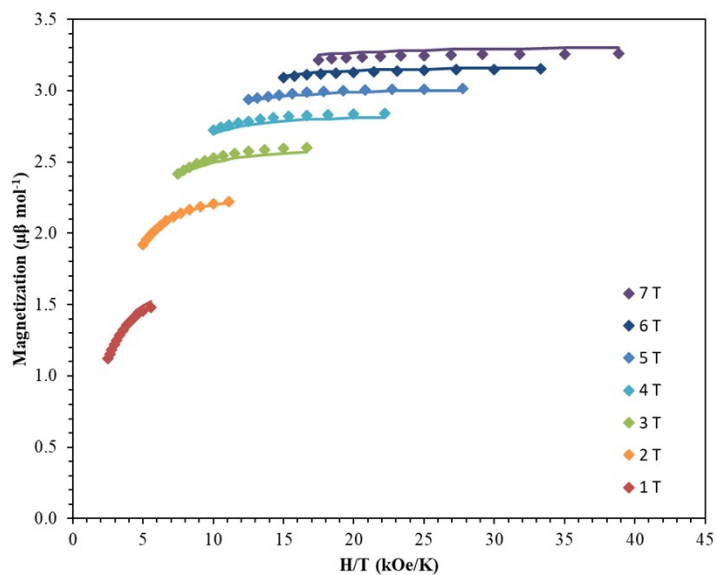


Figure S13. Reduced magnetization for **4**. Solid lines are fits to the experimental data using PHF.

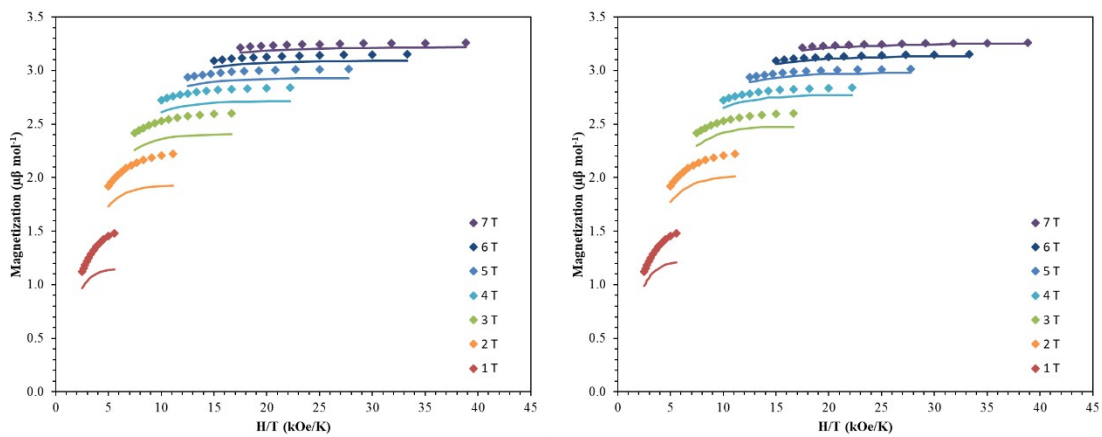


Figure S14. Reduced magnetization for **4**. Solid lines are simulations of CASSCF (left) and NEVPT2 (right) computational results.

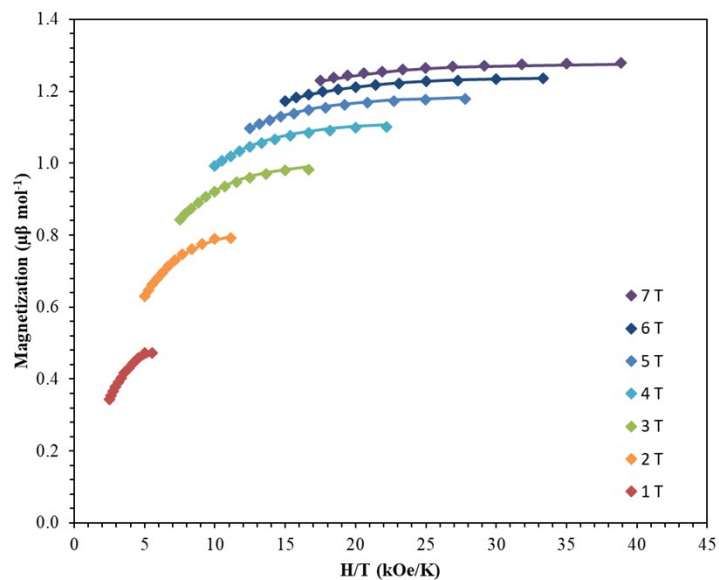


Figure S15. Reduced magnetization for **5**. Solid lines are fits to the experimental data using PHI.

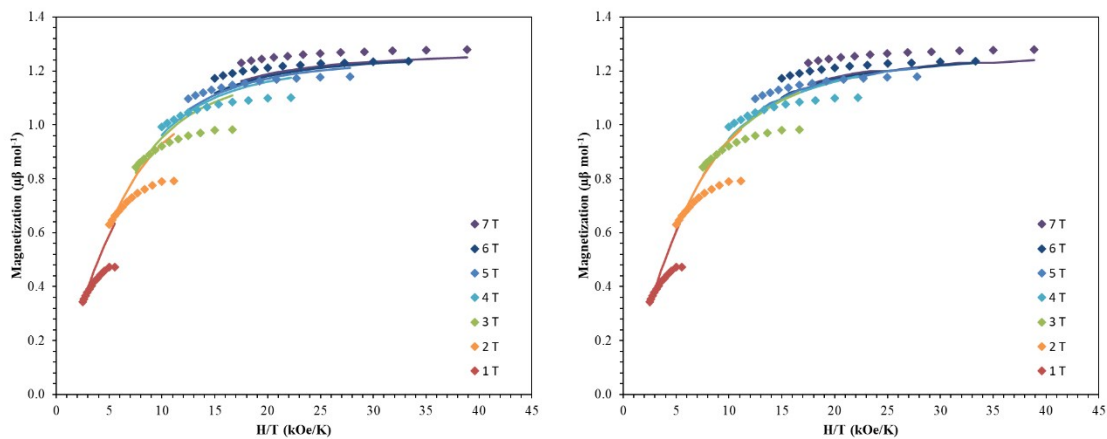


Figure S16. Reduced magnetization for **5**. Solid lines are simulations of CASSCF (left) and NEVPT2 (right) computational results.

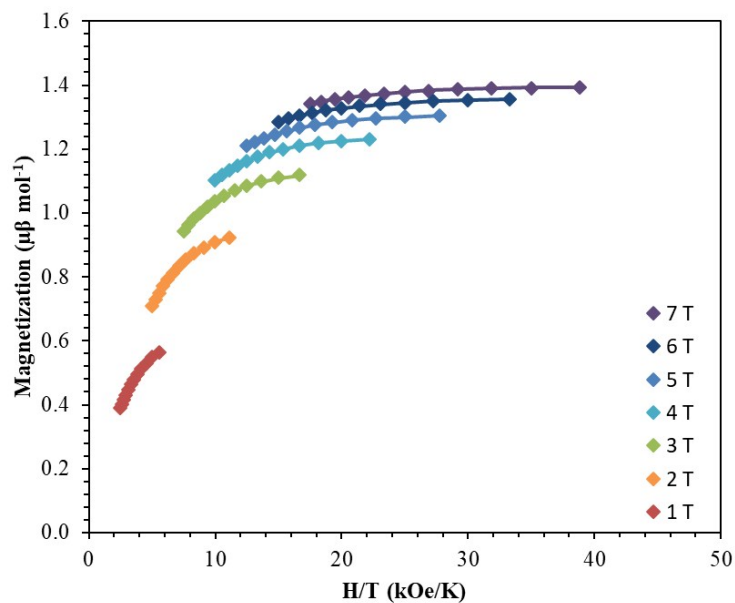


Figure S17. Reduced magnetization for **6**. Solid lines are fits to the experimental data using PHI.

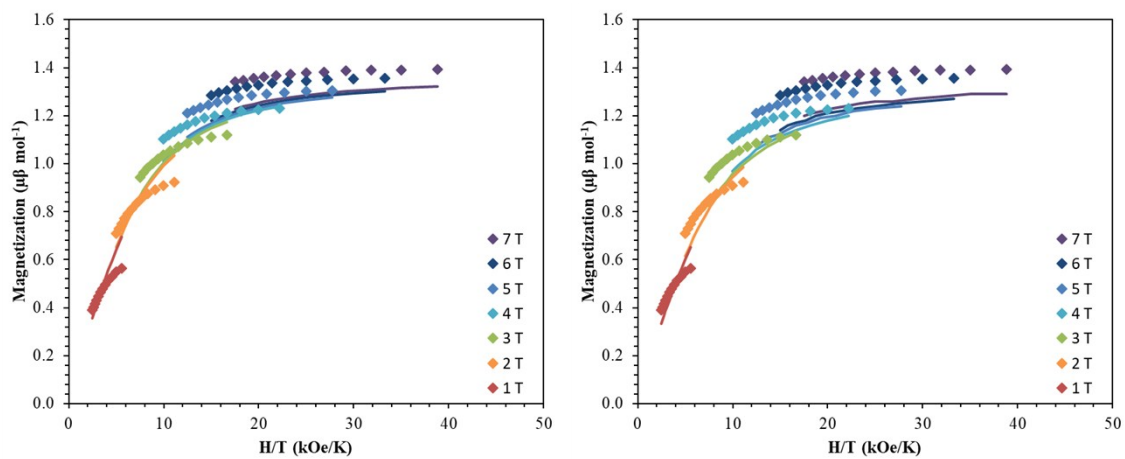


Figure S18. Reduced magnetization for **6**. Solid lines are simulations of CASSCF (left) and NEVPT2 (right) computational results.

In-phase (χ') susceptibility

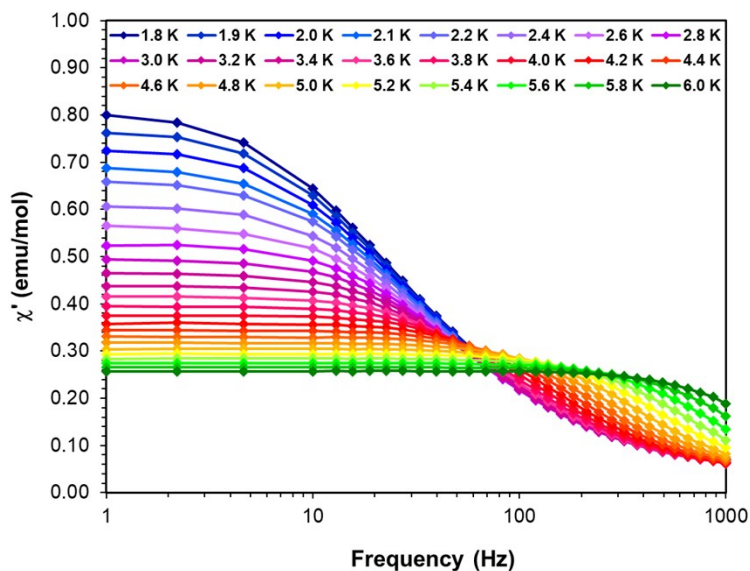


Figure S19. In phase susceptibility (χ') vs Frequency for 1. Solid lines are guides for the eye.

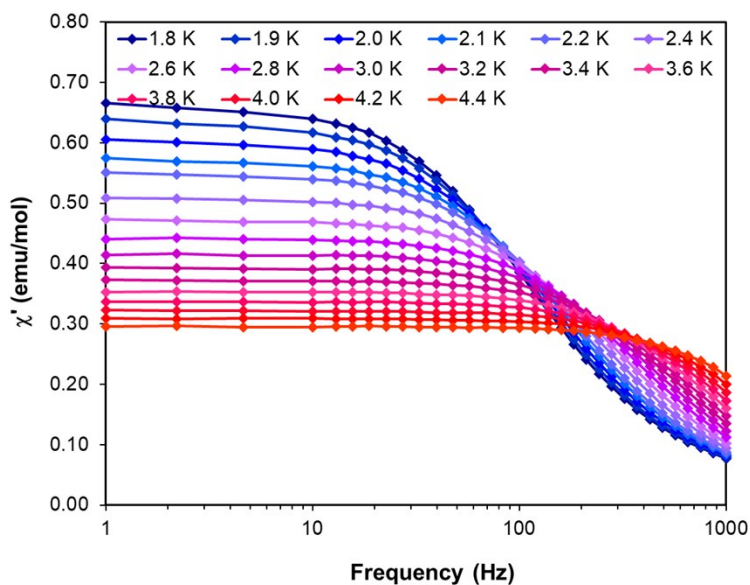


Figure S20. In phase susceptibility (χ') vs Frequency for 2. Solid lines are guides for the eye.

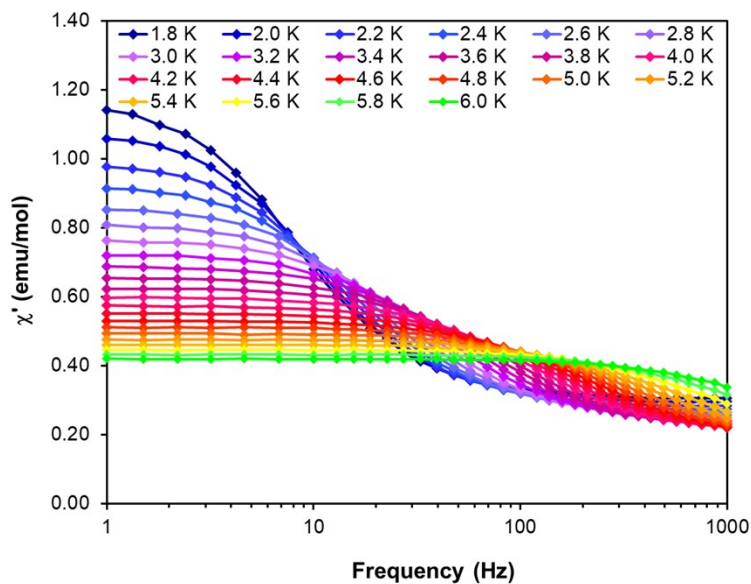


Figure S21. In phase susceptibility (χ') vs Frequency for **3**. Solid lines are guides for the eye.

Cole-Cole plots for 1-3

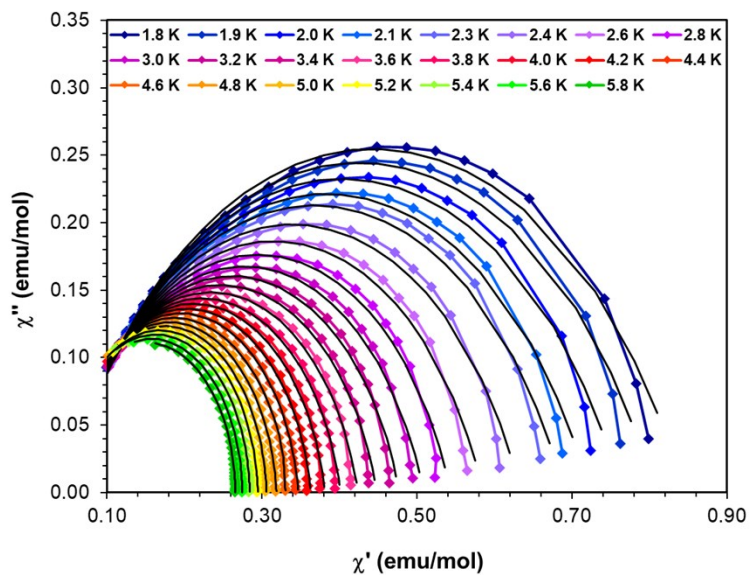


Figure S22. Cole-cole plot for **1**. Colored lines are guides for the eye. Black lines are the fits based on a generalize Debye model using the program CC-fit.

Table S5. Fit parameters from the cole-cole plot for **1** under the frequencies from 1 -1000 Hz within the temperature range 1.8 – 5.6 K.

T(K)	χ_s	χ_{t1}	τ	α	residual
1.8	4.55E-02	8.43E-01	5.54E-03	2.76E-01	1.84E-03
1.9	4.58E-02	8.05E-01	5.15E-03	2.72E-01	1.78E-03
2	4.58E-02	7.63E-01	4.74E-03	2.67E-01	1.67E-03
2.1	4.59E-02	7.21E-01	4.35E-03	2.61E-01	1.43E-03
2.2	4.62E-02	6.89E-01	4.07E-03	2.55E-01	1.41E-03
2.4	4.67E-02	6.33E-01	3.57E-03	2.42E-01	1.36E-03
2.6	4.65E-02	5.86E-01	3.12E-03	2.30E-01	1.09E-03
2.8	4.69E-02	5.44E-01	2.74E-03	2.14E-01	1.04E-03
3	4.64E-02	5.09E-01	2.41E-03	2.01E-01	8.12E-04
3.2	4.62E-02	4.77E-01	2.12E-03	1.85E-01	6.89E-04
3.4	4.57E-02	4.49E-01	1.84E-03	1.69E-01	6.00E-04
3.6	4.54E-02	4.24E-01	1.59E-03	1.52E-01	4.85E-04
3.8	4.49E-02	4.02E-01	1.36E-03	1.35E-01	3.82E-04
4	4.47E-02	3.82E-01	1.15E-03	1.17E-01	3.13E-04
4.2	4.41E-02	3.63E-01	9.59E-04	1.00E-01	2.35E-04
4.4	4.39E-02	3.47E-01	7.94E-04	8.34E-02	1.54E-04
4.6	4.34E-02	3.32E-01	6.51E-04	6.91E-02	1.11E-04
4.8	4.30E-02	3.19E-01	5.26E-04	5.52E-02	7.27E-05
5	4.27E-02	3.06E-01	4.19E-04	4.09E-02	5.60E-05
5.2	4.24E-02	2.95E-01	3.31E-04	3.04E-02	3.30E-05
5.4	4.12E-02	2.85E-01	2.56E-04	2.36E-02	2.01E-05
5.6	4.03E-02	2.75E-01	1.95E-04	1.85E-02	1.26E-05
5.8	3.98E-02	2.66E-01	1.46E-04	1.11E-02	1.34E-05

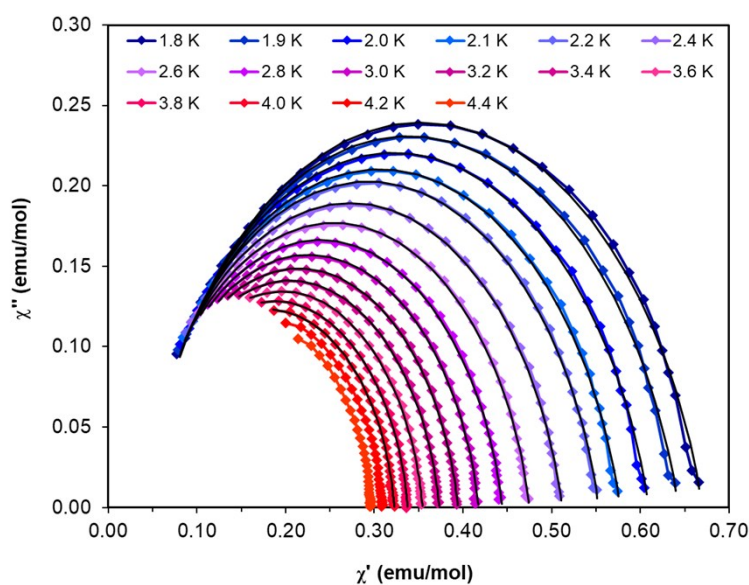


Figure S23. Cole-cole plot for **2**. Colored lines are guides for the eye. Black lines are the fits based on a generalize Debye model using the program CC-fit.

Table S6. Fit parameters from the cole-cole plot for **2** under the frequencies from 1 -1000 Hz within the temperature range 1.8 – 4.0 K.

T(K)	χ_s	χ_{t1}	τ	α	residual
1.8	3.74E-02	6.70E-01	1.34E-03	1.75E-01	3.28E-04
1.9	3.66E-02	6.43E-01	1.21E-03	1.71E-01	3.02E-04
2	3.56E-02	6.09E-01	1.05E-03	1.66E-01	2.41E-04
2.1	3.49E-02	5.77E-01	9.11E-04	1.60E-01	1.78E-04
2.2	3.43E-02	5.53E-01	8.10E-04	1.56E-01	1.54E-04
2.4	3.40E-02	5.12E-01	6.54E-04	1.47E-01	1.31E-04
2.6	3.38E-02	4.75E-01	5.29E-04	1.39E-01	1.06E-04
2.8	3.39E-02	4.44E-01	4.35E-04	1.33E-01	9.50E-05
3	3.48E-02	4.18E-01	3.62E-04	1.25E-01	9.99E-05
3.2	3.52E-02	3.95E-01	3.03E-04	1.20E-01	7.49E-05
3.4	3.64E-02	3.73E-01	2.55E-04	1.12E-01	6.62E-05
3.6	3.78E-02	3.55E-01	2.16E-04	1.04E-01	6.04E-05
3.8	3.94E-02	3.38E-01	1.83E-04	9.60E-02	5.41E-05
4	4.01E-02	3.22E-01	1.53E-04	8.74E-02	4.69E-05

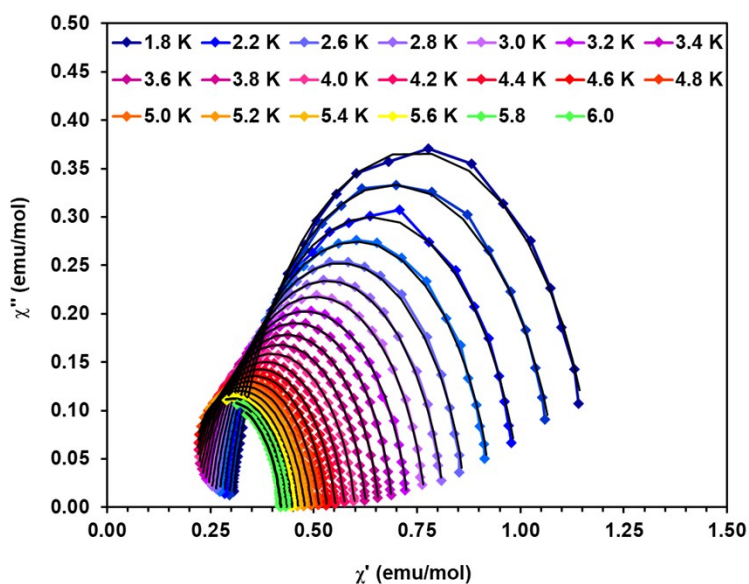


Figure S24. Cole-cole plot for **3**. Colored lines are guides for the eye. Black lines are the fits based on a generalize Debye model using the program CC-fit.

Table S7. Fit parameters from the cole-cole plot for **3** under the frequencies from 1 -1000 Hz within the temperature range 1.8 – 5.6 K.

T(K)	χ_s	χ_{t1}	τ	α	residual
1.8	3.04E-01	1.18E+00	1.87E-02	1.14E-01	1.25E-03
2	2.93E-01	1.09E+00	1.56E-02	1.16E-01	8.17E-04
2.2	2.81E-01	1.00E+00	1.24E-02	1.18E-01	8.54E-04
2.4	2.70E-01	9.33E-01	9.88E-03	1.19E-01	4.88E-04
2.6	2.59E-01	8.69E-01	7.76E-03	1.19E-01	4.08E-04
2.8	2.50E-01	8.16E-01	6.06E-03	1.20E-01	2.73E-04
3	2.40E-01	7.70E-01	4.74E-03	1.24E-01	1.44E-04
3.2	2.31E-01	7.28E-01	3.70E-03	1.29E-01	9.29E-05
3.4	2.23E-01	6.91E-01	2.89E-03	1.31E-01	5.32E-05
3.6	2.14E-01	6.57E-01	2.28E-03	1.36E-01	3.75E-05
3.8	2.07E-01	6.27E-01	1.80E-03	1.41E-01	5.67E-05
4	2.00E-01	6.00E-01	1.44E-03	1.47E-01	6.40E-05
4.2	1.93E-01	5.76E-01	1.15E-03	1.53E-01	7.20E-05
4.4	1.86E-01	5.53E-01	9.21E-04	1.59E-01	6.99E-05
4.6	1.80E-01	5.32E-01	7.36E-04	1.64E-01	7.64E-05
4.8	1.75E-01	5.14E-01	5.83E-04	1.68E-01	9.25E-05
5	1.70E-01	4.95E-01	4.54E-04	1.68E-01	6.74E-05
5.2	1.66E-01	4.79E-01	3.47E-04	1.66E-01	8.00E-05
5.4	1.63E-01	4.63E-01	2.59E-04	1.61E-01	1.13E-04
5.6	1.63E-01	4.48E-01	1.91E-04	1.50E-01	1.25E-04
5.8	1.63E-01	4.34E-01	1.38E-04	1.39E-01	1.13E-04
6	1.62E-01	4.21E-01	9.71E-05	1.26E-01	9.07E-05

Computational details

Ab initio calculations based on the wave function theory approach were used to compute the ZFS of Co^{II}, Fe^{II}, and Ni^{II} ions in **1–6** using ORCA 3.0 suite of programs.⁹ We employed the BP86 functional along with scalar relativistic ZORA Hamiltonians and def2-TZVP basis sets for the metal ions and the first coordination sphere and def2-SVP for the rest of the atoms. The RI approximation with secondary TZV/J Columbic fitting basis sets were used along with increased integration grids (Grid 5 in ORCA convention). The tight SCF convergence was used throughout the calculations (1×10^{-8} Eh). The SOC contributions in the *ab initio* framework were obtained using second-order perturbation theory as well as by employing the effective Hamiltonian approach, which enables calculations of all matrix elements to be made of the anisotropic spin Hamiltonian from the *ab initio* energies and wave functions numerically. Here we have employed the state average-CASSCF (Complete Active Space Self-Consistent Field) method to compute the ZFS. The active space comprises of seven active electrons in five active d-orbitals (d⁷ system; CAS (7,5)) for Co^{II} ion, six active electrons in five active d-orbitals (d⁶ system; CAS (6,5)) for Fe^{II} ion and eight active electrons in five active d-orbitals (d⁸ system; CAS (8,5)) for Ni^{II} ion. With this active space, we computed all of the 10 quartet and 40 doublet states for Co^{II} ion, 5 quintet and 45 triplet states for Fe^{II} ion, and 10 triplet and 15 singlet states for Ni^{II} ion in the configuration interaction procedure.¹⁰ In addition to the converged CASSCF wave function, we performed NEVPT2 (n-electron valence state perturbation theory) calculations to treat the dynamical correlations.¹¹

$$\hat{H}_{so} = \sum_i \xi_i \left(\lambda_{zi} \hat{s}_{zi} + \frac{1}{2} (\lambda_{+i} \hat{s}_{-i} + \lambda_{-i} \hat{s}_{+i}) \right) \quad (1)$$

The sign and the magnitude of D values are rationalized using the spin-orbit operator (Eq.1). When

a spin-allowed excitation of β -electron between orbitals with same $|\pm m_l|$ levels, the $\sum_i \lambda_{zi} \hat{s}_{zi}$ operator couples those orbitals and leads to a negative D value. Conversely, when such an

excitation occurs between orbitals with different $|\pm m_l|$ levels, the $\frac{1}{2} \sum_i (\lambda_{+i} \hat{s}_{-i} + \lambda_{-i} \hat{s}_{+i})$ operator couples those orbitals and leads to a positive D value.¹²

Table S8. CASSCF (NEVPT2) computed energies (cm^{-1}) and contributions to D value from the first four excited states for **1** – **6** along with the g_x , g_y and g_z values from the effective Hamiltonian.

Complex	g_x, g_y, g_z	Excited state	Energy	D Contribution
1	2.00, 2.35, 2.36 (2.00, 2.25, 2.26)	First	4811.3 (4731.5)	17.1 (12.0)
		Second	4972.8 (4894.5)	16.3(11.5)
		Third	5706.6 (5562.3)	-0.6 (-0.4)
		Fourth	5738.5 (5594.2)	-0.1(-0.1)
2	2.09, 2.31, 2.34 (2.07, 2.23, 2.25)	First	3384.0 (3381.9)	-3.7 (-2.6)
		Second	4054.2 (4105.6)	-0.1(-0.1)
		Third	4870.8 (4912.1)	13.1 (9.4)
		Fourth	5204.3 (5219.2)	12.6 (8.9)
3	1.83, 1.89, 2.56 (1.85, 1.92, 2.54)	First	874.9 (879.2)	-36.0 (-33.9)
		Second	5650.5 (5643.4)	2.5 (2.0)
		Third	6962.3 (6959.0)	0.7 (0.6)
		Fourth	7126.2 (7132.9)	0.6 (0.5)
4	2.03, 2.09, 2.19 (2.02, 2.07, 2.15)	First	1284.6 (1346.2)	4.1 (3.3)
		Second	4617.8 (4622.5)	-1.1 (-0.9)
		Third	5393.8 (5499.3)	1.2 (0.9)
		Fourth	8814.1 (8711.7)	1.6 (1.2)
5	1.85, 1.85, 3.75 (1.79, 1.80, 3.73)	First	77.6 (77.7)	-530.8 (-500.0)
		Second	5671.8 (5688.1)	34.3 (23.6)
		Third	5763.7 (5775.8)	13.1 (8.3)
		Fourth	5987.5 (6002.5)	15.4 (11.1)
6	2.13, 2.16, 3.25 (2.13, 2.15, 2.96)	First	244.3 (253.2)	-264.0 (-186.6)
		Second	6494.9 (6522.1)	24.6 (17.2)
		Third	7384.7 (7380.3)	21.6 (15.3)
		Fourth	9036.9 (9011.6)	7.1 (4.8)

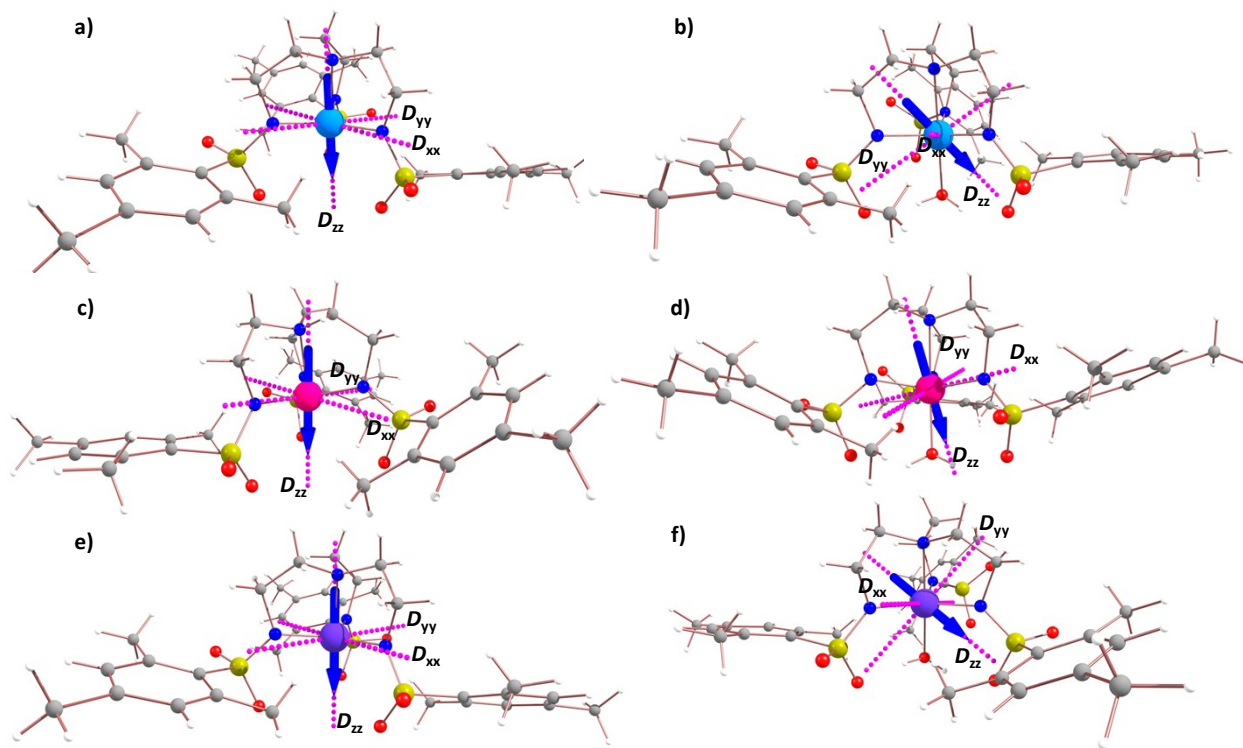


Figure S25. CASSCF computed D_{xx} , D_{yy} , and D_{zz} axes (pink dotted lines) for a) 1 b) 2 c) 3 d) 4 e) 5 f) 6. The blue arrow emphasizes the direction and orientation of the D_{zz} axis.

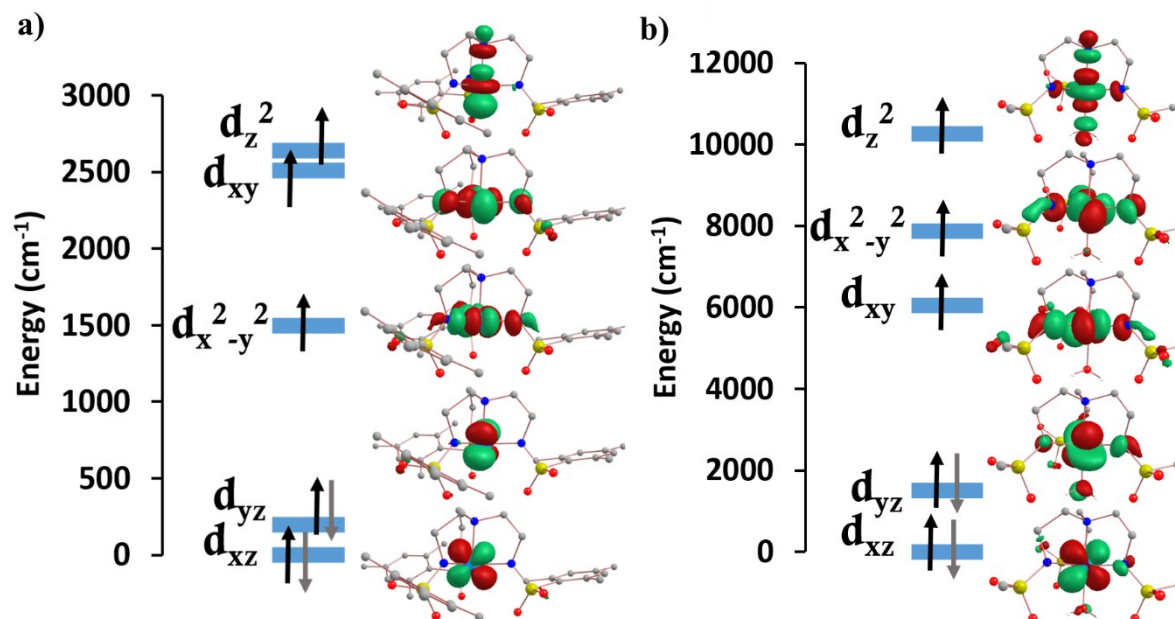


Figure S26. CASSCF-computed d-orbital ordering for complex a) 1 and b) 2.

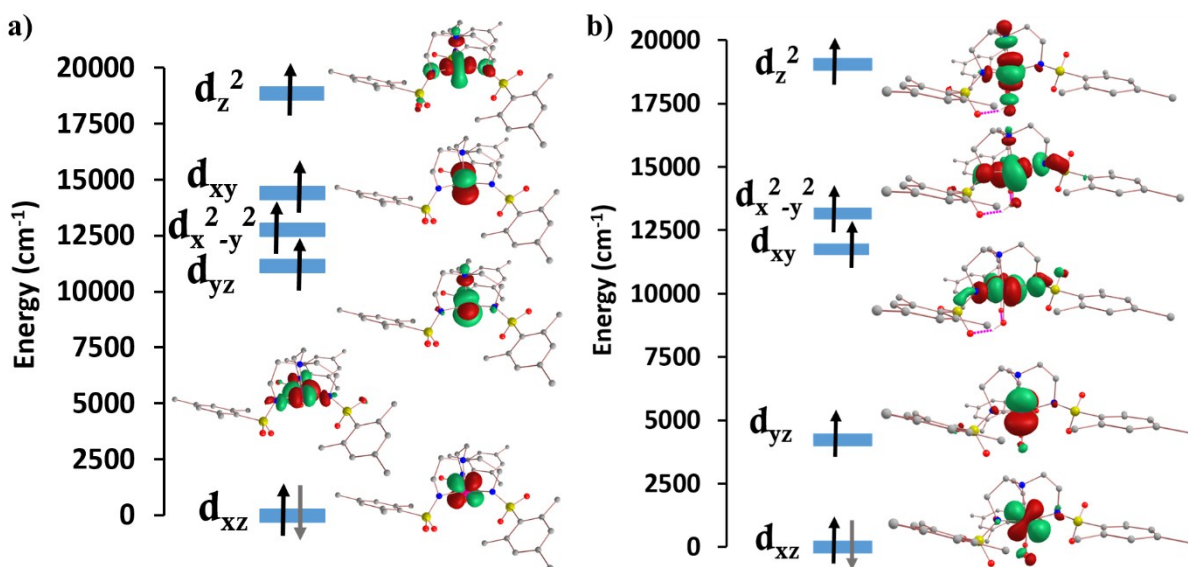


Figure S27. CASSCF-computed d-orbital ordering for complexes a) **3** and b) **4**.

We performed additional calculations on compound **5** considering relativistic ZORA basis sets to the def2-TZVP/def2-SVP basis sets to see the effect on the Hamiltonian parameters. The resulting values are tabulated below. The results indicate that the relativistic effect can be added either to the effective Hamiltonian or to the basis sets in these complexes.

Table S9. CASSCF (NEVPT2) computed g_x , g_y and g_z , D and E/D values along with energies and contributions to D value from first four excited states for **5**.

g_x, g_y, g_z	D (cm ⁻¹)	E/D	Excited state	Energy (cm ⁻¹)	D Contribution
1.85, 1.85, 3.75	433.9	0.6	First	77.0 (77.1)	-531.3 (-500.5)
(1.79, 1.79, 3.73)	(428.6)	(0.001)	Second	5301.5 (5320.3)	34.5 (23.8)
			Third	5511.7 (5533.3)	12.9 (8.4)
			Fourth	5761.4 (5779.5)	13.7 (9.8)

References

1. D. C. Lacy, Y. J. Park, J. W. Ziller, J. Yano and A. S. Borovik, *J. Am. Chem. Soc.*, 2012, **134**, 17526-17535.
2. Y. J. Park, S. A. Cook, N. S. Sickerman, Y. Sano, J. W. Ziller and A. S. Borovik, *Chem. Sci.*, 2013, **4**, 717-726.
3. S. A. Cook, J. W. Ziller and A. S. Borovik, *Inorg. Chem.*, 2014, **53**, 11029-11035.
4. *APEX2*, v2013.10-0; Bruker AXS: Madison, WI, **2013**.
5. G. Sheldrick, *Acta Crystallogr., Sect. A: Found. Crystallogr.* 2008, **64**, 112.
6. G. Sheldrick, *Acta Crystallogr., Sect. A: Found. Adv.* 2015, **71**, 3.
7. Dolomanov, O.V., Bourhis, L.J., Gildea, R.J., Howard, J.A.K. & Puschmann, H. *J. Appl. Cryst.* 2009, **42**, 339.
8. G. A. Bain and J. F. Berry, *J. Chem. Ed.* 2008, **85**, 532.
9. F. Neese, *WIREs Comput. Mol. Sci.* 2012, **2**, 73-78.
10. F. Weigend, R. Ahlrichs, *Phys. Chem. Chem. Phys.* 2005, **7**, 3297-3305.
11. a) C. Angeli, R. Cimiraglia, J.-P. Malrieu, *Chem. Phys. Lett.* 2001, **350**, 297-305; b) C. Angeli, R. Cimiraglia, J. P. Malrieu, *Chem. Phys. Lett.* 2001, **350**, 297-305; c) C. Angeli, R. Cimiraglia, J. P. Malrieu, *J. Chem. Phys.* 2002, **117**, 9138-9153.
12. a) S. Gomez-Coca, E. Cremades, N. Aliaga-Alcalde, E. Ruiz, *J. Am. Chem. Soc.* 2013, **135**, 7010-7018; b) T. J. Woods, M. F. Ballesteros-Rivas, S. Gómez-Coca, E. Ruiz, K. R. Dunbar, *J. Am. Chem. Soc.* 2016, **138**, 16407-16416.